

Towards real-world navigation with deep differentiable planners

Shu Ishida João F. Henriques
Visual Geometry Group, University of Oxford
{ishida, joao}@robots.ox.ac.uk

August 13, 2021

Abstract

We train embodied neural networks to plan and navigate unseen complex 3D environments, emphasising real-world deployment. Rather than requiring prior knowledge of the agent or environment, the planner learns to model the state transitions and rewards. To avoid the potentially hazardous trial-and-error of reinforcement learning, we focus on differentiable planners such as Value Iteration Networks (VIN), which are trained offline from safe expert demonstrations. Although they work well in small simulations, we address two major limitations that hinder their deployment. First, we observed that current differentiable planners struggle to plan long-term in environments with a high branching complexity. While they should ideally learn to assign low rewards to obstacles to avoid collisions, we posit that the constraints imposed on the network are not strong enough to guarantee the network to learn sufficiently large penalties for every possible collision. We thus impose a structural constraint on the value iteration, which explicitly learns to model any impossible actions. Secondly, we extend the model to work with a limited perspective camera under translation and rotation, which is crucial for real robot deployment. Many VIN-like planners assume a 360 degrees or overhead view without rotation. In contrast, our method uses a memory-efficient lattice map to aggregate CNN embeddings of partial observations, and models the rotational dynamics explicitly using a 3D state-space grid (translation and rotation). Our proposals significantly improve semantic navigation and exploration on several 2D and 3D environments, succeeding in settings that are otherwise challenging for this class of methods. As far as we know, we are the first to successfully perform differentiable planning on the difficult Active Vision Dataset, consisting of real images captured from a robot.

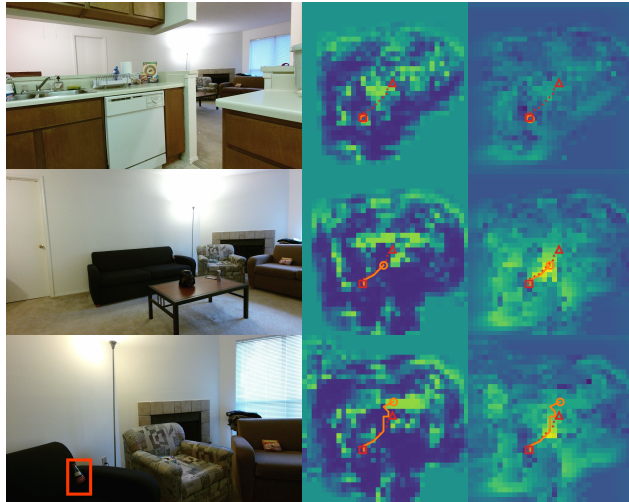


Figure 1: (**1st column**) Input images seen during a run of our method on AVD (sec. 5.2.2). This embodied neural network has learned to efficiently explore and navigate unseen indoor environments, to seek objects of a given class (highlighted in the last image). (**2nd-3rd columns**) Predicted rewards and values (respectively), for each spatial location (higher for brighter values). The unknown optimal trajectory is dashed, while the robot’s trajectory is solid.

1 Introduction

Continuous advances in robotics have enabled robots to be deployed to a wide range of scenarios, from manufacturing in factories and cleaning in households, to the emerging applications of autonomous vehicles and delivery drones [1]. Improving their autonomy is met with many challenges, due to the difficulty of planning from uncertain sensory data. In classical robotics, the study of planning has a long tradition [2], using detailed knowledge of a robot’s configuration and sensors, with little emphasis on learning from data. An almost orthogonal approach is to use deep learning, an intensely data-driven, non-parametric approach [3]. Modern deep neural networks excel at pattern recognition [4], although they do not offer a direct path to planning applications. While one approach would be to parse a scene into pre-defined elements (e.g. object classes and their poses) to be passed to a more classical planner, an end-to-end approach where all modules are learnable has the chance to improve with data, and be adaptable to novel settings with no manual tuning. Because of the data-driven setup, a deep network has the potential to learn behaviour that leverages the biases and characteristics of the environment. For example, while the best generic strategy to reach the exit in a maze may be to follow a wall on one side, a better one for office buildings could be to first exit any room and then follow the corridors to the end [1]. Value Iteration Networks (VINs) [5] emerged as an elegant way to merge classical planning and data-driven deep networks,

by defining a *differentiable* planner. Being sub-differentiable, like all other elements of a deep network, allows the planner to include learnable elements, trained end-to-end from example data. For example, it can learn to identify and avoid obstacles, and to recognise and seek classes of target objects, without examples labelled explicitly. However, there are many gaps between VIN’s idealised formulation and realistic robotics scenarios. The original formulation for navigation [5] considers that the full environment is visible and expressible as a 2D grid. As such, it does not account for limited embodied (first-person) observations in 3D spaces, unexplored and partially-visible environments, or the mismatch between egocentric observations and idealised world-space discrete states.

In this paper we address these challenges, and close the gap between current differentiable planners and realistic robot navigation applications. Our contributions are:

1. A constrained transition model for value iteration, following a rigorous probabilistic formulation, which explicitly models illegal actions and task termination (sec. 4.1).
2. A 3D state-space grid that supports embodied planning through the robot’s translation and rotation (sec. 4.2.1). As far as we know, we are the first to experiment with differentiable planners beyond 2D translation.
3. A trajectory reweighting scheme that addresses the unbalanced nature of navigation training distributions (sec. 4.1.5).
4. An efficient representation that fuses observations of the same spatial location across time and space (different points-of-view), allowing differentiable planners to handle long time-horizons and free-form trajectories (sec. 4.2.2).
5. Experiments showing that our proposals are instrumental to enable differentiable planning in more complex environments than previously. We demonstrate for the first time that they can work on the challenging Active Vision Dataset [6], with image sequences from a real robot platform (sec. 5.2.2).

Sec. 2 discusses related work, while sec. 3 gives a short introduction to differentiable planning. Sec. 4 presents our technical proposals, and sec. 5 evaluates them.

2 Related work

Planning and reinforcement learning. Planning in fully-known deterministic state spaces was partially solved by graph-search algorithms [7, 8, 9, 10, 11, 12]. A Markov Decision Process (MDP) [13, 14] considers probabilistic transitions and rewards, enabling planning on stochastic models and noisy environments. With known MDPs, Value Iteration achieves the optimal solution [13, 14]. Reinforcement Learning (RL) focuses on unknown MDPs. There is a plethora of algorithms for unknown MDPs, such as value-based methods [15, 16], policy-based methods [17, 18], and actor-critic methods [18], often used with deep networks as function approximators. However, these systems are reactive: a

policy (i.e.a generic plan) is built over a long period of trial and error, and will be specific to the training environment (there is no online planning). This makes them less ideal for robotics, where risky failures must be avoided, and new plans (policies) must be created on-the-fly in new environments. When white-box access to a simulator is assumed, Monte Carlo Tree Search [19] is also effective.

Deep networks for navigation. Savinov et al.[20] achieve navigation by composing siamese networks and value estimators trained on proxy tasks. However, it is not trained end-to-end, and requires footage of a walk through the environment to build the initial map. The Neural Map [21] is an A2C [18] agent that reads and writes to a differentiable memory (i.e.a map). However, the policy is reactive (there is no online planning). Similarly, Mirowski et al.[22] train reactive policies which are specific to an environment. The Value Prediction Network [23] learns an MDP and its state-space from data. However, during planning only a single future state is predicted per action, which ignores stochastic environments. Its memory and computation scale exponentially with planning depth, so only short plans are considered. Hausknecht et al. [24] add recurrence to deep Q-learning to address partially-observable environments, however only single-frame occlusions are considered.

Imitation learning. To avoid learning by trial-and-error, Imitation Learning instead uses expert trajectories. Inverse Reinforcement Learning (IRL) [25, 26, 27, 28] achieves this by learning a reward function that best explains the expert trajectories. However, this generally leads to a difficult nested optimisation and is an ill-posed problem, since many reward functions can explain the same trajectory.

Differentiable planning. Tamar et al.[5] introduced the Value Iteration Network (VIN) for Imitation Learning, which generates a plan online (with value iteration) and back-propagates errors through the plan to train estimators of the rewards (see sec. 3.1). Lee et al. [29] replaced the maximum over actions in the VI formula with a LSTM. The evaluation included extension to rotation, but assuming a fully-known four directional view for every gridded state. VINs were applied to localisation from partial observations by Karkus et al.[30], but assuming a full map of the environment.

Most previous work on deploying VIN to robots [31, 32] have assumed an occupancy map and goal map rather than learning the map embedding and goal themselves from data. To the best of our knowledge, Gupta et al.[33] is the only work which evaluated a VIN-like differential planner on real-world data using map embeddings learned end-to-end. Their work uses hierarchical VIN to plan on larger environments, and handles rotation as a warping operation external to the VIN and updates an egocentric map. While this is a valid approach, warping an egocentric map per update can result in rapid blurring of the embeddings, and the VIN itself cannot plan rotations in future steps. Gupta et al. only evaluated their method for rotations of 90° and deterministic motion, rather than noisy translation and rotation.

3 Background

A Markov Decision Process (MDP) [13, 14] formalises sequential decision-making. It consists of states $s \in \mathcal{S}$ (e.g.locations), actions available at each state $a \in \mathcal{A}(s)$, a reward function $R(s, a, s')$ to be maximised (e.g.reaching the target), and a transition probability $P(s'|s, a)$ (the probability of the next state s' given the current state s and action a). The objective of an agent is to learn a policy $\pi(a|s)$, specifying the probability of choosing action a for any state s , chosen to maximise the expected return G_t at every time step t . A return is a sum of discounted rewards, $G_t = \sum_{k=0}^{\infty} \gamma^k R_{t+k+1}$, where a discount factor $\gamma \in (0, 1)$ prevents divergences of the infinite sum. The value function $V_{\pi}(s) = \mathbb{E}_{\pi}[G_t|s_t = s]$ evaluates future returns from a state, while the action-value function $Q_{\pi}(s, a) = \mathbb{E}_{\pi}[G_t|s_t = s, a_t = a]$ considers both a state and the action taken. An optimal policy π_* should then maximise the expected return for all states, i.e. $\forall s \in \mathcal{S}, v_*(s) = \max_{\pi} v_{\pi}(s)$. Value Iteration (VI) [13, 14] is an algorithm to obtain an optimal policy, by alternating a refinement of both value (V) and action-value (Q) function estimates in each iteration k . When s and a are discrete, $Q^{(k)}$ and $V^{(k)}$ can be implemented as simple tables (tensors). In particular, we will consider as states the cells of a 2D grid, corresponding to discretised locations in an environment, i.e. $s = (i, j) \in \mathcal{S} = \{1, \dots, N\}^2$. Furthermore, transitions are local (only to coordinates offset by $s' \in K = \{-1, 0, 1\}^2$):

$$Q_{a,s}^{(k)} = \sum_{s' \in K} P_{a,s',s} \left(R_{a,s',s} + \gamma V_{s+s'}^{(k-1)} \right)$$

$$\forall a \in \mathcal{A}(s), \quad \text{with} \quad V_s^{(k)} = \max_{a \in \mathcal{A}(s)} Q_{a,s}^{(k)}, \quad (1)$$

Note that to avoid repetitive notation s and s' are 2D indices, so V is a 2D matrix and both R and P are 5D tensors. The policy $\pi_s^{(k)} = \operatorname{argmax}_{a \in \mathcal{A}} Q_{a,s}^{(k)}$ simply chooses the action with the highest action-state value. While the sum in eq. 1 resembles a convolution, the filters (P) are space-varying (depend on $s = (i, j)$), so it is not directly expressible as such. Equation 1 represents the “ideal” VI for local motion on a 2D grid, without further assumptions.

3.1 Value Iteration Network

While VI guarantees the optimal policy, it requires that the functions for transition probability P and reward R are known (e.g.defined by hand). Tamar et al.[5] pointed out that all VI operations are (sub-)differentiable, and as such a model of P and R can be *trained from data* by back-propagation. For the case of planning on a 2D grid (navigation), they related eq. 1 to a CNN, as:

$$Q_{a,s}^{(k)} = \sum_{s' \in K} \left(P_{a,s'}^R \hat{R}_{s+s'} + P_{a,s'}^V V_{s+s'}^{(k-1)} \right),$$

$$\forall a \in \mathcal{A}, \quad \text{with} \quad V_s^{(k)} = \max_{a \in \mathcal{A}} Q_{a,s}^{(k)}, \quad (2)$$

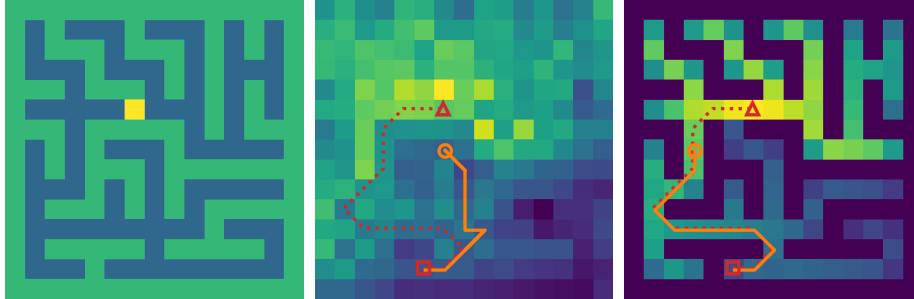


Figure 2: **(left)** A 2D maze, with the target in yellow. **(middle)** Values produced by the VIN for each 2D state (actions are taken towards the highest value). Higher values are brighter. The correct trajectory is dashed, the current one is solid. The agent (orange circle) is stuck due to the local maximum below it. **(right)** Same values for our method, CALVIN. There are no spurious maxima, and the values of walls are correctly considered low (dark).

where $P^R, P^V \in \mathbb{R}^{A \times |K|}$ are two learned convolutional filters that represent the transitions (P in eq. 1), and \hat{R} is a predicted 2D reward map. Note that \mathcal{A} is independent of s , i.e.all actions are allowed in all states. This turns out to be detrimental (see next paragraph). The reward map \hat{R} is predicted by a CNN, from an input of the same size that represents the available observations. In Tamar et al.’s experiments [5], the observations were a fully-visible overhead image of the environment, from which negative rewards such as obstacles and positive rewards such as navigation targets can be located. Each action channel in \mathcal{A} corresponds to a move in the 2D grid, typically 8-directional or 4-directional. Eq. 2 is attractive, because it can be implemented as a CNN consisting of alternating convolutional layers (Q) and max-pooling along the actions (channels) dimension (V).

Motivating experiment. Since the VIN allows all actions at all states (\mathcal{A} does not depend on s), collisions must be modelled as states with low rewards. In practice, the VIN does not learn to forbid such actions completely, resulting in propagation of values from states which cannot be reached directly due to collision along the way. We verified this experimentally, by training a VIN according to Tamar et al. [5] on 4K mazes (see sec. 5 for details). We then measured, for each state, whether the predicted scores for all valid actions are larger than those for all invalid actions (i.e.collisions). If they are, then the network will always avoid collisions. Surprisingly, we found that this was not true for 24.6% of the states. For a real-world robot to work reliably, this is an unacceptably high chance of collisions. As a comparison, for our method (sec. 4) this rate is only 1.6%. In the same experiment, the VIN often gets trapped in local minima of the value function and does not move (fig. 2), which is another failure mode. We aim to fix these issues, and push VINs towards realistic scenarios.

4 Proposed method

We propose a transition model that learns and disallows illegal actions. We also extend the state-space to rotations and incorporate distant observations into a spatial map of embeddings, both necessary for real 3D environments.

4.1 Augmented navigation state-action space

In this section we will derive a probabilistic transition model from first principles, with only two assumptions and no extra hyper-parameters. The first assumption is locality and translation invariance of the agent motion, which was introduced in the VIN to allow efficient learning with shared parameters. Unlike the VIN, we will decompose the transition model $P(s'|s, a)$ into two components: the agent motion model $\hat{P}(s' - s|a)$, which is translation invariant and shared across states (depending only on the spatial difference between states $s' - s$); and an observation-dependent predictor $\hat{A}(s, a) \in [0, 1]$ which evaluates whether action a is available from state s , allowing the network to disqualify actions that are illegal.

In robotics, it is essential that the agent understands that the current task has been completed to move on to the next one. Since in small environments there is a high chance that a randomly-acting agent will stumble upon the target, Anderson et al. [1] suggested that an explicit termination action must be taken at the target to finish successfully.

Therefore, in addition to positional states, we assume a success state W (“win”) that is reached only by triggering a termination action D (“done”), and a failure state F (“fail”) that is reached upon triggering an incorrect action. We denote the reward for reaching F as R_F , and the translation-invariant rewards as $\hat{R}(a, s' - s)$. For simplicity, we consider the reward for success a special case of $\hat{R}(a, s' - s)$ where $a = D$ and $s' = W$. With these assumptions, the reward function $R(s, a, s')$ is equivalent to eq. 3:

$$R(s, a, s') = \begin{cases} \hat{R}_F, & s' = F \\ \hat{R}(a, s' - s), & s' \neq F. \end{cases} \quad (3)$$

Together with the agent motion model $\hat{P}(s' - s|a)$, action validity predictor $\hat{A}(s, a)$ and the definition of a failure state F , the transition model $P(s'|s, a)$ can be derived as eq. 4:

$$P(s'|s, a) = \begin{cases} 1 - \hat{A}(s, a), & s' = F \\ \hat{A}(s, a)\hat{P}(s' - s|a), & s' \neq F. \end{cases} \quad (4)$$

From the above, we calculate the reward $R(s, a)$ by marginalising over the

neighbour states s' :

$$\begin{aligned} R(s, a) &= \sum_{s'} P(s'|s, a)R(s, a, s') \\ &= \widehat{R}_F(1 - \widehat{A}(s, a)) + \widehat{A}(s, a) \sum_{s'} \widehat{P}(s' - s|a)\widehat{R}(a, s' - s) \end{aligned} \quad (5)$$

Finally, eq. 5 can be plugged into eq. 1 to obtain our proposed value iteration’s $Q(s, a)$:

$$\begin{aligned} Q(s, a) &= R(s, a) + \gamma \mathbb{I}_{a \in \mathcal{A}} \sum_{s'} P(s'|s, a)V(s') \\ &= R(s, a) + \gamma \widehat{A}(s, a) \mathbb{I}_{a \neq D} \sum_{s'} \widehat{P}(s' - s|a)V(s') \end{aligned} \quad (6)$$

where \mathbb{I} is an indicator function. Equation 5 and eq. 6 essentially express a constrained VI, which models the case of an MDP on a grid with unknown illegal states and termination at a goal state. The inputs to this model are three learnable functions — the motion model $\widehat{P}(s' - s|a)$, the action validity $\widehat{A}(s, a)$ (i.e.obstacle predictions), and the rewards $\widehat{R}(a, s' - s)$ and \widehat{R}_F . These are implemented as CNNs with the observations as inputs (\widehat{R}_F is a single learned scalar). All the constraints follow from a well-defined world-model, with highly interpretable predicted quantities, unlike previous proposals [29, 5]. We named this method Collision Avoidance Long-term Value Iteration Network (CALVIN).

4.1.1 Training

Similarly to Tamar et al. [5], we train our method with a softmax cross-entropy loss L , comparing an example trajectory $\{(s_t, a_t^*) : t \in T\}$ with predicted action scores $Q(s, a)$:

$$\min_{\widehat{P}, \widehat{A}, \widehat{R}} \frac{1}{|T|} \sum_{t \in T} w_t L(Q(s_t), a_t^*), \quad (7)$$

where $Q(s)$ is a vector with one element per action, $Q(s, a)$, and w_t is an optional weight that can be used to bias the loss if $w_t \neq 1$ (sec. 4.1.5). Example trajectories are shortest paths computed from random starting points to the target (also chosen randomly). Note that the learned functions can be conditioned on input observations. These are 2D grids of features, with the same size as the considered state-space (i.e.a map of observations), which is convenient since it enables \widehat{P} , \widehat{A} and \widehat{R} to be implemented as CNNs.

4.1.2 Transition modelling

Similarly to the VIN (eq. 2), the motion model $\widehat{P}(s' - s|a)$ is implemented as a convolutional filter $\widehat{P} \in \mathbb{R}^{|\mathcal{A}| \times |\mathcal{K}|}$, so it only depends on the relative spatial displacement $s' - s$ between the two states s and s' . We can use the transitions already observed in the example trajectory to constrain this model further. For a

given action a , the corresponding filter $\hat{P}(a) \in \mathbb{R}^{|K|}$ should place a probability of 1 on the observed displacement vector $s' - s$, and 0 elsewhere. Formalising this objective, we add a loss term $L(\hat{P}(a_t^*), s_{t+1} - s_t)$ for each step in the example trajectory.

4.1.3 Action availability

Although the available actions \hat{A} could, in theory, be learned completely end-to-end, in practice we found that additional regularisation is necessary. If we had a reliable log-probability of each action being taken, $\hat{A}_{\text{logit}}(s, a)$, then by thresholding it at some point $\hat{A}_{\text{thresh}}(s)$ we would distinguish between available and unavailable actions. Using a sigmoid function σ as a soft threshold, we can write this as:

$$\hat{A}(s, a) = \sigma(\hat{A}_{\text{logit}}(s, a) - \hat{A}_{\text{thresh}}(s)). \quad (8)$$

Both $\hat{A}_{\text{logit}}(s, a)$ and $\hat{A}_{\text{thresh}}(s)$ are predicted by the network, given the observations at each time step. In order to ground the probabilities of each action being taken, $\hat{A}_{\text{logit}}(s, a)$ is trained with an additional cross-entropy loss to predict the probability of taking an action at each state, as in eq. 7. Note that this auxiliary loss does not require any extra supervision or labels – we use strictly the same training data as the VIN.

4.1.4 Fully vs. partially observable environments

Several previous works [5, 29] assume that the entire environment is static and fully observable, which is often unrealistic. Partially observable environments, involving unknown scenes, require exploring to gather information and are thus more challenging. We account for this with a simple but significant modification. Note that $Q(s_t)$ in eq. 7 depends on the learned functions (CNNs) \hat{P} , \hat{A} and \hat{R} through eq. 6, and these in turn are computed from the observations. We extend the VIN framework to the case of partial observations by ensuring that $Q(s_t|O_t)$ depends *only* on the observations up to time t , O_t . This means that the VIN is recomputed from scratch each step t (since the observations are different), instead of just once for a whole trajectory. Locations that were not observed yet have their observed features filled with zeros, so in practice knowledge of the environment is slowly built up during an expert demonstration, which enables exploration behaviour to be learned.

4.1.5 Trajectory reweighting

Exploration (sec. 4.1.4) provides observations O_t of the same locations at different times. We can thus augment eq. 7 to include these partial observations as extra samples, without requiring any additional annotation. The sum in eq. 7 becomes $\sum_{t' \in T} \sum_{t \in T_{1:t'}} w_t L(Q(s_t|O_{t'}), a_t^*)$. For long trajectories, the training data then becomes severely unbalanced between exploration (target not visible) and exploitation (target visible), with a much larger proportion of samples of the former (90% of the data in the environments of sec. 5.1.2). We addressed

this by reweighting the samples. We set $w_t = \beta^{d_t} / \max_{j \in T} \beta^{d_j}$ in eq. 7, i.e.a geometric decay scaling with the topological distance to the target d_t .

4.2 Embodied navigation in 3D environments

Embodied agents such as robots have a pose in 3D space, which for non-holonomic robots limits their available actions (e.g.moving forward or rotating). They may also have a limited sensor suite, such as a perspective camera aimed in one direction, which will limit their observations. Nevertheless, previous work that used VINs [5, 33] did not consider these limitations, which are important for many realistic platforms, and furthermore mimic the constraints of human navigation.

4.2.1 Embodied pose states (position and orientation)

To address the first limitation, we propose to augment the 2D state-space with an extra dimension, which corresponds to Θ discretised orientations: $\mathcal{S} = \{1, \dots, N\}^2 \times \{1, \dots, \Theta\}$. This can be achieved by directly adding one extra dimension to each spatial tensor in eq. 5 and eq. 6. A table of correspondences between tensor dimensions of the positional method and the embodied method can be found in Appendix A. Note that the much larger state-space makes long-term planning more difficult to learn. As far as we are aware, we are the first to experiment with VINs on 3D pose navigation problems.

4.2.2 3D embeddings for geometric reasoning

While the VIN performs its operations on a 2D grid – a discretisation of an absolute (world-centric) reference frame – generally an agent only has access to observations in a local (camera-centric) reference frame. Past work has either considered fixed overhead cameras [5] or local 360° cameras [33, 29]. Of the latter, Lee et al.[29] assume that such images are observed densely at all positions, which can only be assumed in simulation, while Gupta et al.[33] apply the VIN to a local reference frame only, which requires a reprojection of the observations at every step, losing information over time. Instead, we aim to project and accumulate information about local scene observations over time into an absolute reference frame.

Since the learnable functions (\hat{P} , \hat{A} and \hat{R}) in our proposed method (and other VIN-based methods) are 2D CNNs, their natural input is a 2D grid of m -dimensional embeddings, denoted $e_{tij} \in \mathbb{R}^m$, for time t and discrete world-space coordinates (i, j) . This can be interpreted as a spatio-temporal map tensor. We then wish to project and aggregate useful semantic information from an image I_t , extracted by a CNN ϕ , into this tensor. This requires both knowledge of the camera position c_t and rotation matrix R_t , which we assume following previous work [33, 29, 5] (and which can be estimated from monocular vision [34]). Spatial projection also requires knowing (or estimating) the depths $d_t(p)$ of each pixel p in I_t (either with a RGBD camera as in our experiments, or monocular depth estimation [35]). We can then write the homogenous 3D coordinates of each

pixel p in the absolute reference frame using projective geometry [36]:

$$[x_t(p), y_t(p), z_t(p), 1] = c_t + R_t K [p_1, p_2, d_t(p), 1]^\top, \quad (9)$$

where K is the camera’s intrinsics matrix. Given these absolute coordinates of pixel p , we can calculate the closest map embedding e_{tij} to it, and thus aggregate the CNN embeddings $\phi(I_t)$ associated with all pixels close to a map cell. Inspired by PointNet [37], we choose max-pooling for aggregation. Since we have spatial aggregation, we can easily extend this framework to work spatio-temporally, aggregating information from past frames $t' \leq t$. More formally:

$$e_{tij} = \max_{t' \leq t} \{ \phi_p(I_{t'}) : \tau i \leq x_{t'}(p) < \tau(i+1), \tau j \leq y_{t'}(p) < \tau(j+1), p \in I_{t'} \} \quad (10)$$

where τ is the absolute size of each square grid cell, and $\phi_p(I_{t'})$ retrieves the CNN embedding of image $I_{t'}$ for pixel p . Due to the similarity between eq. 10 and a PointNet embedded on a 2D lattice, we named it Lattice PointNet (LPN). Other than the lattice embedding, there are other major differences from the PointNet: we apply it spatio-temporally with a causal constraint ($t' \leq t$), and the downstream predictors that take it as input ($\widehat{P}(e_t)$, $\widehat{A}(e_t)$ and $\widehat{R}(e_t)$) are 2D CNNs that can reason spatially in the lattice, as opposed to the PointNet’s unstructured multi-layer perceptrons [37]. A related proposal for SLAM used spatial max-pooling but more complex LSTMs/GRUs for temporal aggregation [38, 39]. Another related work on end-to-end trainable spatial embeddings uses egospherical memory [40].

The proposed LPN has some appealing properties in our context of navigation: 1) it allows reasoning about far away, observed but yet unvisited locations; 2) it fuses multiple observations of the same location, whether from different points-of-view or different times. In sec. 5 we show that this representation brings a large performance improvement.

Memory-efficient mapping. Since the max operation is permutation-invariant, eq. 10 can be computed recursively as $e_{t,i,j} = \max(e_{t-1,i,j}, e'_{t,i,j})$, where $e'_{t,i,j}$ is computed with eq. 10 but using only the current image I_t . Only the previous map $e_{t-1,i,j}$ must be kept, not all past observations. This means that at run-time the memory cost is *constant* w.r.t. the sequence length, allowing arbitrarily-long operation in principle (unlike methods that need all past observations [20]).

5 Experiments

In this section we will gradually build up the capabilities of our method with the proposals from sec. 4, comparing it to various baselines on increasingly challenging environments, and leading up to unseen real-world 3D environments.

Table 1: Navigation success rate (fraction of trajectories that reach the target) on unseen 2D mazes. Partial observations (exploring an environment gradually) and embodied navigation (translation-rotation state-space) are important yet challenging steps towards full 3D environments.

Environment	Standard loss			Reweighted loss (ours)		
	VIN	GPPN	CALVIN	VIN	GPPN	CALVIN (ours)
Full obs.	0.43	0.95	0.99	0.96	0.99	0.99
Partial obs.	0.06	0.08	0.34	0.01	0.11	0.89
Embodied	0.22	0.21	0.65	0.20	0.23	0.55

5.1 2D grid environments

We start with 2D environments, where the observations are top-down views of the whole scene, and which thus do not require dealing with perspective images (sec. 4.2.2). Since Tamar et al. [5] obtain near-perfect performance in their 2D environments, after reproducing their results we focused on 2D mazes, which are much more challenging since they require frequent backtracking to navigate. The 15×15 mazes are generated using Wilson’s algorithm [41], and an example can be visualised in fig. 3. The allowed moves \mathcal{A} are to any of the 8 neighbours of a cell. As discussed in sec. 4, a termination action D must be triggered at the target to successfully complete the task. The target is placed in a free cell chosen uniformly at random, with a minimum topological distance from the (random) starting location equal to the environment size. We found this necessary to avoid trivial tasks (i.e. starting close to the target).

5.1.1 Fully-known environment with positional states

Baselines and training. For the first experiment, we compare our method (CALVIN) with other differentiable planners: the VIN [5] and the more recent GPPN [29], on fully-observed environments. Other than using mazes instead of convex obstacles, this setting is close to Tamar et al.’s [5]. The VIN, GPPN and CALVIN all use 2-layer CNNs to predict their inputs (details in Appendix A). All networks are trained with $4K$ example trajectories in an equal number of different mazes, using the Adam optimiser with the optimal learning rate chosen from $\{10^{-2}, 10^{-3}, 10^{-4}\}$, until convergence (30 epochs). Since our proposed reweighted loss (sec. 4.1.5) is equally applicable to all differentiable planners, we report results with and without it for all methods.

Results. Table 1 (first row) shows the navigation success rate (fraction of trajectories that reach the target). With the standard loss, the VIN has a very low success rate, showing that it does not scale to large mazes. GPPN achieves a high success rate, and CALVIN performs near-perfectly. This may be explained by the GPPN’s higher capacity, as it contains a LSTM with more parameters. Nevertheless, CALVIN has fewer parameters and a more constrained architecture, so its higher performance hints at a better inductive bias for navigation. It is

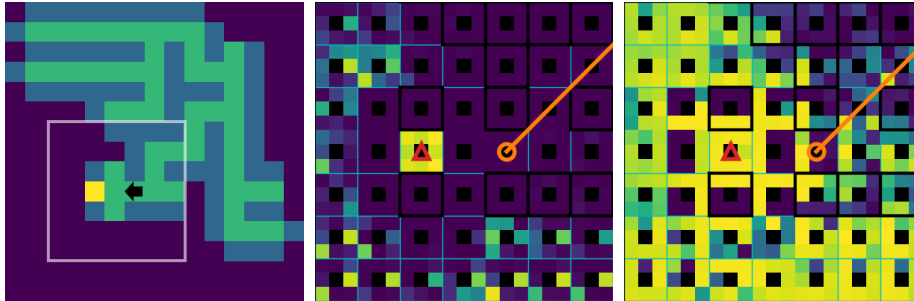


Figure 3: Our method on 2D mazes (sec. 5.1.3). **(left)** Input visualisation: unexplored cells are dark, the target is yellow (just found by the agent), and a black arrow shows the agent’s position and orientation. **(middle)** Close-up of predicted rewards (higher values are brighter) inside the white rectangle of the left panel. The 3D state-space (position/orientation) is shown, with rewards for the 8 orientations in a radial pattern within each cell (position). Explored cells have low rewards, with the highest reward at the target. **(right)** Close-up of predicted values. Values are higher facing the direction of the target. Obstacles (black border) have low values.

interesting to note that the proposed reweighted loss has a beneficial effect on all methods, not just CALVIN. With the correct data distribution, any method with sufficient capacity can fit the objective. This shows that addressing the unbalanced nature of the training data is an important factor, and complementary to other criteria.

5.1.2 Partially observable environment

Setting. Next, we compare the same methods in unknown environments, where the observation maps only contain observed features up to the current time step (sec. 4.1.4). To simulate local observations, we perform ray-casting to identify cells that are visible from the current position, up to 2 cells away. Example observations are in Appendix A.

Results. From table 1 (2nd row) we can see that partial observability causes most methods to fail catastrophically. The sole exception is CALVIN with the reweighted loss (proposed), which performs relatively well. Note that to succeed, an agent must acquire several complex behaviours: directing exploration to the largest unseen areas; backtracking from dead ends; deciding when to backtrack early to a more promising region (and whether the lost time is worth it); and seeking the target when seen. Our method displays all of these behaviours (see Appendix A for visualisations). While the model initially assigns high values to all unexplored states, as soon as the target is in view, the model assigns a high value to the target state and its neighbours. Since only a combination of CALVIN and a reweighted loss works at all, we infer that a correct inductive bias and a balanced data distribution are both necessary for success.

Table 2: Navigation success rate on unseen 3D mazes (MiniWorld). Most methods do not generalise to larger mazes.

Size	CNN backbone		LPN backbone (ours)		
	A2C	PPO	VIN	GPPN	CALVIN (ours)
3×3	0.59	0.37	0.95	0.95	0.99
8×8	0.18	0.07	0.32	0.18	0.69

5.1.3 Embodied navigation with orientation

Setting. Now we consider embodied navigation, in which possible transitions depend on the agent’s orientation (sec. 4.2.1). We augment the state-space of all methods according to sec. 4.2.1, with 8 orientations at 45° intervals, and allow 4 move actions \mathcal{A} : forward, backward, and rotating in either direction.

Results. In table 1 (3rd row) we observe that VIN and GPPN perform slightly better, but still have a low chance of success. CALVIN outperforms them by a large margin. It is interesting to note that, unlike CALVIN, the reweighted loss does not improve the results in this setting. We hypothesize that this is due to the small environment size resulting in more even balance of explored/unexplored cells. We also visualise a typical run in fig. 3. Please refer to the caption for more detailed analysis. One advantage of CALVIN displayed in fig. 3 and fig. 2 is that values and rewards are fully interpretable and play the expected roles in value iteration (eq. 1). Less constrained architectures [5, 29] insert operators that deviate from the value iteration formulation, and thus lose their interpretability as rewards and values (c.f. Appendix A).

5.2 3D environments

Having validated embodied navigation and exploration, we now integrate the Lattice PointNet (LPN, sec. 4.2.2) to handle first-person views of 3D environments.

5.2.1 Synthetically-rendered environments

Dataset. We used the MiniWorld simulator [42], which allowed us to easily generate 3D maze environments with arbitrary layouts. Only a monocular camera is considered (not 360° views [29]). The training trajectories now consist of first-person videos of the shortest path to the target, visualised in fig. 4. We generate mazes on either small (3×3) or large (8×8) grids by adding or removing walls at the boundaries of this grid’s cells. Note that the maze’s layout and the agent’s location do not necessarily align with the 2D grids used by the planners (unlike [29]). Thus, planning happens on a fine discretisation of the state-space (30×30 for small mazes and 80×80 for large ones, with 8 orientations). This allows smooth motions and no privileged information about the specifics of the environment. Both translation and rotation are perturbed by Gaussian noise, forcing all agents to model uncertain dynamics.

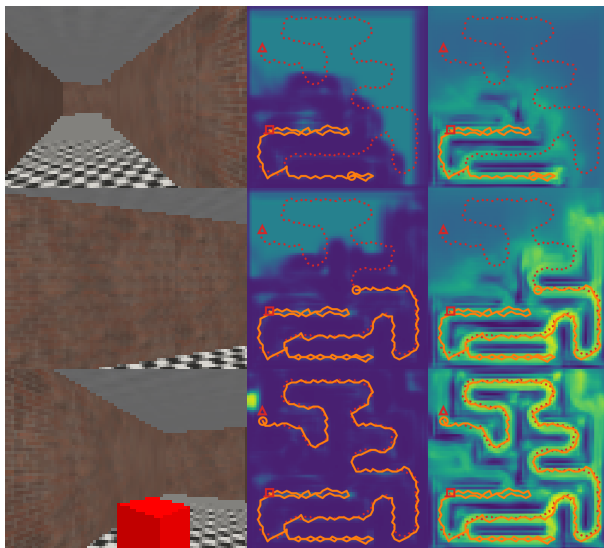


Figure 4: Example run of our method on MiniWorld (sec. 5.2.1). From left to right: input images, predicted rewards and values. The format is the same as for fig. 1. Notice the high reward on unexplored regions, replaced with a single peak around the target when it is seen (last row).

Baselines and training. We compare several baselines: two popular RL methods, A2C [18] and PPO [43], as well as the VIN, GPPN and the proposed CALVIN. All methods use as a first stage a simple 4-layer CNN (details in Appendix A). Since this CNN was not enough to get the VIN, GPPN and CALVIN to work well (see Appendix A), they all use our proposed LPN backbone. We could not include GPPN’s strategy of taking as input views at all possible states [29], due to the high memory requirements and the environment not being fully visible (only local views are available). Other training details are identical to sec. 5.1.

Results. In table 2 we observe that, although the RL methods are successful in small mazes, their reactive policies cannot scale to large mazes. CALVIN succeeds reliably even for longer trajectories, outperforming the others. It is interesting to note that the proposed LPN backbone is important for all differentiable planners, and it allows them to achieve very high success rates for small environments (though our CALVIN method performs slightly better). We show an example run of our method in fig. 4, where it found the target after an efficient exploration period, despite not knowing its location and never seeing this maze before.

5.2.2 Indoor images from a real-world robot

Finally, we tested our method on real images obtained with a robotic platform.

Dataset. We used the Active Vision Dataset [6] (AVD), which allows interactive navigation with real image streams, without synthetic rendering (as opposed

Table 3: Navigation success rate on the Active Vision Dataset, consisting of real robot images taken in indoor environments. The task is to navigate to an object of a learned class, or to an object given an example image. All methods use our LPN backbone, as they fail without it.

Subset	Class-based navigation			Example-based navigation		
	VIN	GPPN	CALVIN	VIN	GPPN	CALVIN (ours)
Training	0.93	0.68	0.96	0.58	0.39	0.61
Validation	0.47	0.66	0.68	0.31	0.34	0.53

to [44]). This is achieved using monocular RGBD images from 19 indoor environments, densely collected by a robot on a 30cm grid and at 30° rotations. The set of over 15K images can be composed to simulate any trajectory, up to the some spatial granularity. There are also bounding box annotations of object instances, which we use to evaluate semantic navigation. We use the last two environments as a validation set, and the rest for training (by sampling 1K shortest paths to the target). A visualisation is shown in fig. 1.

Tasks and training. We considered two semantic navigation tasks: seeking an object of a learned class, and seeking an object given an example image of it. The first is the most similar to the previous settings, seeking the most common class (“soda bottle”). The second requires a separate stream to process the target image, consisting of the first 2 blocks of a ResNet18 pre-trained on ImageNet. This embedding is then concatenated to the main CNN backbone’s output, which has the same architecture. Training follows sec. 5.2.1.

Results. The RL baselines failed on AVD, so we report the performances of VIN, GPPN and CALVIN in table 3. As in sec. 5.2.1, they also fail without our LPN ($\simeq 0\%$ success rate), so all results are with the LPN backbone. A similar conclusion to that for synthetic environments can be drawn: proper spatio-temporal aggregation of local observations is essential for differentiable planners to scale realistically. On class-based navigation, both VIN and CALVIN achieve high accuracy on the training set, but only CALVIN maintains its performance on the validation set, evidencing a lack of generalisation by the VIN. The GPPN has worse training performance than CALVIN and VIN, but the validation performance outperforms VIN, showing that it can indeed process realistic scenes better than VIN, when using a strong representation (our LPN). On example-based navigation, CALVIN outperforms them by a wide margin, especially on the validation set. This shows that CALVIN learns effective generic strategies to seek a specific object, unlike VIN and GPPN which overfit to the layout and appearance of the training environments.

6 Conclusion

We analysed several shortcomings of current differentiable planners, with the goal of deploying to real robot platforms. We found that they can be addressed

by highly complementary solutions: a constrained transition model (CALVIN) correctly incorporates illegal actions (as opposed to simply discouraging them via rewards); a 3D state-space accounts for robot orientation; a LPN backbone efficiently fuses spatio-temporal information; and trajectory reweighting addresses unbalanced training data. We provide empirical evidence in several settings, demonstrating that these all contribute to successful embodied navigation, especially on images from a real robot. Future work may include more complex tasks, such as natural language commands, and study the effect of drift on navigation performance.

References

- [1] P. Anderson, A. Chang, D. S. Chaplot, A. Dosovitskiy, S. Gupta, V. Koltun, J. Kosecka, J. Malik, R. Mottaghi, M. Savva *et al.*, “On evaluation of embodied navigation agents,” *arXiv preprint arXiv:1807.06757*, 2018.
- [2] S. Thrun, “Probabilistic robotics,” *Communications of the ACM*, vol. 45, no. 3, pp. 52–57, 2002.
- [3] I. Goodfellow, Y. Bengio, A. Courville, and Y. Bengio, *Deep learning*. MIT press Cambridge, 2016, vol. 1, no. 2.
- [4] A. Sharif Razavian, H. Azizpour, J. Sullivan, and S. Carlsson, “Cnn features off-the-shelf: an astounding baseline for recognition,” in *Proceedings of the IEEE conference on computer vision and pattern recognition workshops*, 2014, pp. 806–813.
- [5] A. Tamar, Y. WU, G. Thomas, S. Levine, and P. Abbeel, “Value Iteration Networks,” in *Advances in Neural Information Processing Systems 29*, D. D. Lee, M. Sugiyama, U. V. Luxburg, I. Guyon, and R. Garnett, Eds., 2016, pp. 2154–2162.
- [6] P. Ammirato, P. Poirson, E. Park, J. Kosecka, and A. C. Berg, “A dataset for developing and benchmarking active vision,” *arXiv preprint arXiv:1702.08272*, 2017.
- [7] E. W. Dijkstra, “A note on two problems in connexion with graphs,” *Numerische Mathematik*, 1959.
- [8] P. E. Hart, N. J. Nilsson, and B. Raphael, “A formal basis for the heuristic determination of minimum cost paths,” *IEEE Transactions on Systems Science and Cybernetics*, 1968.
- [9] A. Stentz, “Optimal and Efficient Path Planning for Partially-Known Environments,” in *Proceedings of the International Conference on Robotics and Automation*, 1994, p. 8.

- [10] L. Kavraki, P. Svestka, J. Latombe, and M. Overmars, “Probabilistic roadmaps for path planning in high-dimensional configuration spaces,” *IEEE Transactions on Robotics and Automation*, 1996.
- [11] S. M. Lavalle, “Rapidly-exploring random trees: A new tool for path planning,” *Computer Science Department, Iowa State University*, 1998.
- [12] S. M. Lavalle and J. James J. Kuffner, “Rapidly-exploring random trees - progress and prospects,” *Algorithmic and Computational Robotics: New Directions*, 2000.
- [13] R. Bellman, “A Markovian Decision Process,” *Indiana University Mathematics Journal*, vol. 6, no. 4, pp. 679–684, 1957.
- [14] R. S. Sutton and A. G. Barto, *Reinforcement Learning: An Introduction*, 2nd ed. MIT Press, 2018.
- [15] C. Watkins, “Learning From Delayed Rewards,” Ph.D. dissertation, University of Cambridge, Jan. 1989.
- [16] G. A. Rummery and M. Niranjan, “Online Q-learning using Connectionist Systems,” *Department of Engineering, University of Cambridge*, p. 21, 1994.
- [17] R. J. Williams, “Simple Statistical Gradient-Following Algorithms for Connectionist Reinforcement Learning,” in *Machine Learning*, 1992, pp. 229–256.
- [18] V. Mnih, A. P. Badia, M. Mirza, A. Graves, T. Lillicrap, T. Harley, D. Silver, and K. Kavukcuoglu, “Asynchronous Methods for Deep Reinforcement Learning,” in *Proceedings of the International Conference on Machine Learning*, Jun. 2016, pp. 1928–1937, nOOPissn: 1938-7228 Section: Machine Learning.
- [19] D. Silver, A. Huang, C. J. Maddison, A. Guez, L. Sifre, G. v. d. Driessche, J. Schrittwieser, I. Antonoglou, V. Panneershelvam, M. Lanctot, S. Dieleman, D. Grewe, J. Nham, N. Kalchbrenner, I. Sutskever, T. Lillicrap, M. Leach, K. Kavukcuoglu, T. Graepel, and D. Hassabis, “Mastering the game of Go with deep neural networks and tree search,” *Nature*, vol. 529, no. 7587, pp. 484–489, Jan. 2016, number: 7587 Publisher: Nature Publishing Group.
- [20] N. Savinov, A. Dosovitskiy, and V. Koltun, “Semi-parametric Topological Memory for Navigation,” *International Conference on Learning Representations (ICLR)*, Mar. 2018.
- [21] E. Parisotto and R. Salakhutdinov, “Neural map: Structured memory for deep reinforcement learning,” *arXiv preprint arXiv:1702.08360*, 2017.
- [22] P. Mirowski, R. Pascanu, F. Viola, H. Soyer, A. J. Ballard, A. Banino, M. Denil, R. Goroshin, L. Sifre, K. Kavukcuoglu, D. Kumaran, and R. Hadsell, “Learning to Navigate in Complex Environments,” *arXiv:1611.03673 [cs]*, Jan. 2017, arXiv: 1611.03673.

- [23] J. Oh, S. Singh, and H. Lee, “Value prediction network,” in *Advances in Neural Information Processing Systems*, 2017, pp. 6118–6128.
- [24] M. Hausknecht and P. Stone, “Deep recurrent q-learning for partially observable mdps,” *arXiv preprint arXiv:1507.06527*, 2015.
- [25] A. Y. Ng and S. J. Russell, “Algorithms for Inverse Reinforcement Learning,” in *Proceedings of the International Conference on Machine Learning*, ser. ICML ’00, San Francisco, CA, USA, Jun. 2000, pp. 663–670.
- [26] B. D. Ziebart, A. Maas, J. A. Bagnell, and A. K. Dey, “Maximum Entropy Inverse Reinforcement Learning,” *AAAI Conference on Artificial Intelligence*, p. 6, 2008.
- [27] B. D. Ziebart, J. A. Bagnell, and A. K. Dey, “Modeling Interaction via the Principle of Maximum Causal Entropy,” in *27th International Conference on Machine Learning*, 2010, p. 8.
- [28] J. Ho and S. Ermon, “Generative Adversarial Imitation Learning,” in *Advances in Neural Information Processing Systems 29*, D. D. Lee, M. Sugiyama, U. V. Luxburg, I. Guyon, and R. Garnett, Eds., 2016, pp. 4565–4573.
- [29] L. Lee, E. Parisotto, D. S. Chaplot, E. Xing, and R. Salakhutdinov, “Gated Path Planning Networks,” *arXiv:1806.06408 [cs, stat]*, Jun. 2018, arXiv: 1806.06408.
- [30] P. Karkus, D. Hsu, and W. S. Lee, “QMDP-Net: Deep Learning for Planning under Partial Observability,” in *Advances in Neural Information Processing Systems 30*, I. Guyon, U. V. Luxburg, S. Bengio, H. Wallach, R. Fergus, S. Vishwanathan, and R. Garnett, Eds., 2017, pp. 4694–4704.
- [31] D. Schleich, T. Klamt, and S. Behnke, “Value iteration networks on multiple levels of abstraction,” *Robotics: Science and Systems XV*, Jun 2019.
- [32] B. Nie, Y. Gao, Y. Mei, and F. Gao, “Capability iteration network for robot path planning,” *International Journal of Robotics and Automation*, vol. 36, no. 0, 2021.
- [33] S. Gupta, V. Tolani, J. Davidson, S. Levine, R. Sukthankar, and J. Malik, “Cognitive Mapping and Planning for Visual Navigation,” in *Proceedings of the IEEE Conference on Computer Vision and Pattern Recognition*, 2017, arXiv: 1702.03920.
- [34] R. Mur-Artal and J. D. Tardos, “ORB-SLAM2: an Open-Source SLAM System for Monocular, Stereo and RGB-D Cameras,” *IEEE Transactions on Robotics*, vol. 33, no. 5, pp. 1255–1262, Oct. 2017, arXiv: 1610.06475.

- [35] H. Fu, M. Gong, C. Wang, K. Batmanghelich, and D. Tao, “Deep ordinal regression network for monocular depth estimation,” in *Proceedings of the IEEE Conference on Computer Vision and Pattern Recognition*, 2018, pp. 2002–2011.
- [36] R. Hartley and A. Zisserman, “Multiple view geometry in computer,” *Vision, 2nd ed.*, New York: Cambridge, 2003.
- [37] R. Q. Charles, H. Su, M. Kaichun, and L. J. Guibas, “PointNet: Deep Learning on Point Sets for 3D Classification and Segmentation,” in *2017 IEEE Conference on Computer Vision and Pattern Recognition (CVPR)*. Honolulu, HI: IEEE, Jul. 2017, pp. 77–85.
- [38] J. F. Henriques and A. Vedaldi, “MapNet: An Allocentric Spatial Memory for Mapping Environments,” in *2018 IEEE/CVF Conference on Computer Vision and Pattern Recognition*, Jun. 2018, pp. 8476–8484, nOOPissn: 1063-6919.
- [39] V. Cartillier, Z. Ren, N. Jain, S. Lee, I. Essa, and D. Batra, “Semantic mapnet: Building allocentric semantic maps and representations from egocentric views,” 2021.
- [40] D. J. Lenton, S. James, R. Clark, and A. Davison, “End-to-end egospheric spatial memory,” in *International Conference on Learning Representations*, 2021.
- [41] D. B. Wilson, “Generating random spanning trees more quickly than the cover time,” in *Proceedings of the ACM symposium on Theory of Computing*, ser. STOC '96, Philadelphia, Pennsylvania, USA, Jul. 1996, pp. 296–303.
- [42] M. Chevalier-Boisvert, “gym-miniworld environment for openai gym,” <https://github.com/maximecb/gym-miniworld>, 2018.
- [43] J. Schulman, F. Wolski, P. Dhariwal, A. Radford, and O. Klimov, “Proximal policy optimization algorithms,” *ArXiv*, vol. abs/1707.06347, 2017.
- [44] Manolis Savva*, Abhishek Kadian*, Oleksandr Maksymets*, Y. Zhao, E. Wijmans, B. Jain, J. Straub, J. Liu, V. Koltun, J. Malik, D. Parikh, and D. Batra, “Habitat: A Platform for Embodied AI Research,” in *Proceedings of the IEEE/CVF International Conference on Computer Vision (ICCV)*, 2019.

Appendix A

A.1 Implicit assumptions of the VIN architecture

Differences between VIN and the idealised VI on a grid. Comparing eq. 1 in sec. 3 to eq. 2 in sec. 3.1, we note several differences:

1. The VIN value estimate V takes the maximum action-value Q across *all possible actions* \mathcal{A} , even illegal ones (e.g. moving into an obstacle). Similarly, the Q estimate is also updated even for illegal actions. In contrast, VI only considers legal actions for each state (cell), i.e. $\mathcal{A}(i, j)$.
2. The VIN reward \hat{R} is assumed independent of the action. This means that, for example, a transition between two states cannot be penalised directly; a penalty must be assigned to one of the states (regardless of the action taken to enter it).
3. The VIN transition probability is expanded into 2 terms, P^R which affects the reward and P^V which affects the estimated values. This decoupling means that they do not enjoy the physical interpretability of VI’s P (i.e. probability of state transitions), and rewards and values can undergo very different transition dynamics.
4. Unlike the VI, the VIN considers the state transition translation-invariant. This means that it cannot model obstacles (illegal transitions) using P , and must rely on assigning a high penalty to the reward \hat{R} of those states instead.

A.2 Implementation details

A.2.1 Embodied pose states

One of our contributions is extending the VIN framework to accommodate embodied pose states, i.e. states which encode both position and orientation. We achieve this by augmenting the 2D state-space with an extra dimension for orientations. Table 4 shows correspondences between tensor dimensions of the positional method and the embodied method for each component of the architecture. X and Y are the size of the internal spatial discretisation of the environment, M is the internal discretisation of the orientation, A is the number of actions, and K is the kernel dimension for spatial locality.

Note that the value iteration step in CALVIN performs a 2D convolution of \hat{P} over a 2D value map in the case of positional states and a 3D convolution over a 3D value map with orientation in the case of embodied pose states. In the embodied case, the second dimension of \hat{P} corresponds to the orientation of the current state, and the third dimension corresponds to that of the next state.

A.2.2 Architectural design of Lattice PointNet

The Lattice PointNet described in sec. 4.2.2 consists of three stages: a CNN that extracts embeddings from observations in image-space (image encoder), a spatial aggregation step (eq. 10 in sec. 4.2.2) that performs max pooling of embeddings for each map cell, and another CNN that refines the map embedding (map

Table 4: Comparison of individual components in the implementation of CALVIN for positional states and for embodied pose states.

	Positional	Embodied
State s	(x, y)	(θ, x, y)
VI step	Conv2d	Conv3d
$V(s)$	$X \times Y$	$M \times X \times Y$
$Q(s, a)$	$A \times X \times Y$	$A \times M \times X \times Y$
$\hat{A}(s, a)$	$A \times X \times Y$	$A \times M \times X \times Y$
\hat{P}	$A \times K \times K$	$A \times M \times M \times K \times K$
\hat{R}	$A \times K \times K$	$A \times M \times M \times K \times K$

encoder). The image encoder consists of two CNN blocks, each consisting of the following layers in order: batch normalisation, 2D convolution, dropout, ReLU and 2D max pooling. The map encoder consists of 2D convolution, dropout, ReLU, batch normalisation, and finally, another 2D convolution. The number of channels of each convolutional layer are (40, 20, 20, 20), respectively. The point clouds can consume a significant amount of memory for long trajectories. Hence, we sub-sampled the point embeddings to 50000 points after the image encoding step.

The input to the LPN is a 3-channel RGB image for the MiniWorld experiment, and a 128-channel embedding extracted using the first 2 blocks of ResNet18 pre-trained on ImageNet for the AVD experiment. For example-based navigation, an additional input of an example target image is given. We extract the ResNet18 embeddings for the target image, pass both the agent observation embeddings and the target embeddings through a 1×1 convolutional layer and then take the dot product between the observation embeddings and the target embeddings. The dot product channel is then passed through another 1×1 CNN and added to the output of the image encoder. This allows the network to learn the association between the target embedding and the observation embedding.

A.2.3 Architectural design of the CNN backbone

This CNN backbone is used in a control experiment in appendix A.4.2 to show the effectiveness of the LPN backbone. In contrast to LPN which performs spatial aggregation of embeddings, the CNN backbone is a direct application of an encoder-decoder architecture that transforms image-space observations into map-space embeddings. Gupta et al.[33] employed a similar architecture to obtain their map embeddings. While they use ResNet50 as the encoder network, we used a simple CNN for the MiniWorld experiment to match the result obtained with LPN.

The CNN backbone consists of three stages: a CNN encoder, two fully-connected layers with ReLU to transform embeddings from image-space to map-space, and a CNN decoder. The encoder consists of 3 blocks of batch normalisation, 2D convolution, dropout, ReLU and 2D max pooling, and a final

block with just batch normalisation and 2D convolution. The number of channels of each convolutional layer are (64, 128, 128, 128), respectively.

The fully-connected layers take in an input size of $128 \times 5 \times 7$, reduces it to a hidden size of 128, and outputs either $128 \times 5 \times 5$ for the smaller maze or $128 \times 4 \times 4$ for the larger maze, which is then passed to the decoder.

The decoder consists of 3 blocks of batch normalisation, 2D deconvolution, dropout and ReLU, and a final block with just 2D deconvolution. The number of channels of each deconvolution layers are (128, 128, 64, 20), respectively. The output size of the decoder depends on the map resolution, hence we chose appropriate strides, kernel sizes and paddings in the decoder network to match the output sizes of 30×30 and 80×80 . This approach is not scalable to maps with high resolution or with arbitrary size, which is one of the drawbacks of this approach.

A.3 Experiment setup

A.3.1 Expert trajectory generation

Expert trajectories are generated by running an A* [8] planner from the start state to the target state. We assigned Euclidean costs to every transition in the 2D grid environments, and a cost of 1 per move for the MiniWorld and AVD environments. In the case of MiniWorld, an additional cost is assigned to locations near obstacles to ensure that the trajectories are not in close proximity to the walls.

A.3.2 Hyperparameter choices

Similarly to VIN [5] which uses a 2-layer CNN to predict the reward map, and GPPN [29], which uses a 2-layer CNN to produce inputs to the LSTM, CALVIN uses a 2-layer CNN as an available actions predictor $\hat{A}(s, a)$. For each experiment, we chose the size of the hidden layer from {40, 80, 150}. For GPPN, 150 yielded the best results consistently. For VIN and CALVIN, 150 was used for all the grid environments, and 40 for MiniWorld and AVD, which yielded better navigation performance, presumably because the map embeddings are already learnt by the LPN.

VIN has an additional hyperparameter for the number of hidden action channels, which we set to 40, which is sufficiently bigger than the number of actual actions in all of our experiments. While the kernel size K for VIN and CALVIN were set to 3 for experiments in the grid environment, it was noted in [29] that GPPN works better with larger kernel size. Therefore, we chose the best kernel size out of {3, 5, 7, 9, 11} for GPPN. For experiments on MiniWorld and AVD, there are state transitions with step size of 2, hence we chose $K = 5$ for VIN and CALVIN.

The number of value iteration steps k was chosen from {20, 40, 60, 80, 100}. For trajectory reweighting, β was chosen from {0.1, 0.25, 0.5, 0.75, 1.0}.

A.3.3 Rollout at test time

We test the performance of the model by running navigation trials (rollouts) on a randomly generated environment. At every time step, the model is queried the set of Q -values $\{Q(s, a) : a \in \mathcal{A}\}$ for the current state s , and an action which gives the maximum predicted Q value is taken.

While VIN is trained with $V^{(0)}$ initialised with zeros, in a true Value Iteration algorithm, the value function must converge for an optimal policy to be obtained. To help the value function converge faster under a time and compute budget, we initialise the value function with predicted values from the previous time step at test time with online navigation.

We set a limit to the maximum number of steps taken by the agent, which were 200 for the fully-known 15×15 grid, 500 for the partially known grid, 300 for MiniWorld (3×3), 1000 for MiniWorld (8×8), and 100 for AVD.

A.4 Additional experiments

A.4.1 Ablation study of removing loss components

CALVIN is trained on three additive loss components: a loss term for the predicted Q -values L_Q (sec.4.1.1), a loss term for the transition models L_P (sec.4.1.2), and a loss term for the action availability L_A (sec.4.1.3). We assessed the contribution of each loss component to the overall performance.

We conducted the experiments on the partially observable grid environment (sec.5.1.2). The results in table 5 indicate that all loss components, in particular the transition model loss, contributes to the robust performance of the network.

Table 5: Navigation success rate of CALVIN in partially observable 2D mazes with loss components removed.

Loss	$L_Q + L_P + L_A$	$L_Q + L_P$	$L_Q + L_A$
Success rate	0.88	0.82	0.08

A.4.2 Comparison of LPN against CNN backbone

We compared our proposed LPN backbone against a typical encoder-decoder CNN backbone as a component that maps observations to map embeddings. We evaluated the performance of the two methods for VIN, GPPN and CALVIN. In table 6, we observe that LPN backbone is highly effective, especially for larger environments where long-term planning based on spatially aggregated embeddings is necessary.

A.5 Learnt noisy transition model

CALVIN explicitly learns the transition model $\hat{P}(s' - s|a)$ from expert trajectories. We confirm that this learning mechanism works even for transitions with added

Table 6: Navigation success rate on unseen 3D mazes (MiniWorld). Most methods do not generalise to larger mazes. The proposed LPN demonstrates robust performance in larger unseen mazes.

Size	CNN backbone			LPN backbone (ours)		
	VIN	GPPN	CALVIN	VIN	GPPN	CALVIN
3×3	0.89	0.73	0.75	0.95	0.95	0.99
8×8	0.00	0.18	0.08	0.32	0.18	0.69

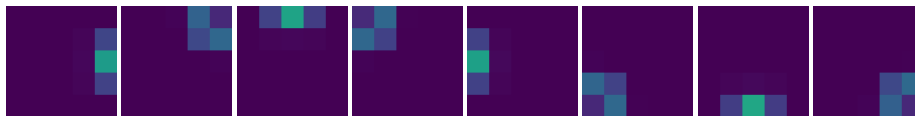


Figure 5: Transition model learnt from MiniWorld trajectories for the *move forward* action at each discretised orientation at 45° intervals. Higher values are brighter (yellow for a probability of 1), and lower values are darker (purple for a probability of 0).

noise, which is the case for MiniWorld experiments. Figure 5 visualises the learnt state transitions for the *move forward* action. We observe that the network is able to model the noise added to transitions and propagate values probabilistically from the possible next states.

A.6 Example rollout in a partially observable maze

We present an example of a trajectory taken by CALVIN at runtime, with corresponding observation maps and predicted values in Figure 6. At each rollout step, CALVIN performs inference on the best action to take based on its current observation map. No information about the location of the target is given until it is within view of the agent. This makes the problem challenging, since the agent may have to take significantly more steps compared to an optimal route to reach the target. In this example, the agent managed to backtrack every time it encountered a dead end, successfully reaching the target after 65 steps. The model initially assigns high values to all unexplored states. When the target comes into view, the model assigns a high probability to the availability of the “done” action at the corresponding state. The agent learns a sufficiently high reward for a successful termination so that the “done” action is triggered at the target.

A.7 Comparison of embodied navigation

For visual comparison of CALVIN, VIN and GPPN, we generated a maze and performed rollouts using each of the algorithms, assuming partial observability and embodied navigation.

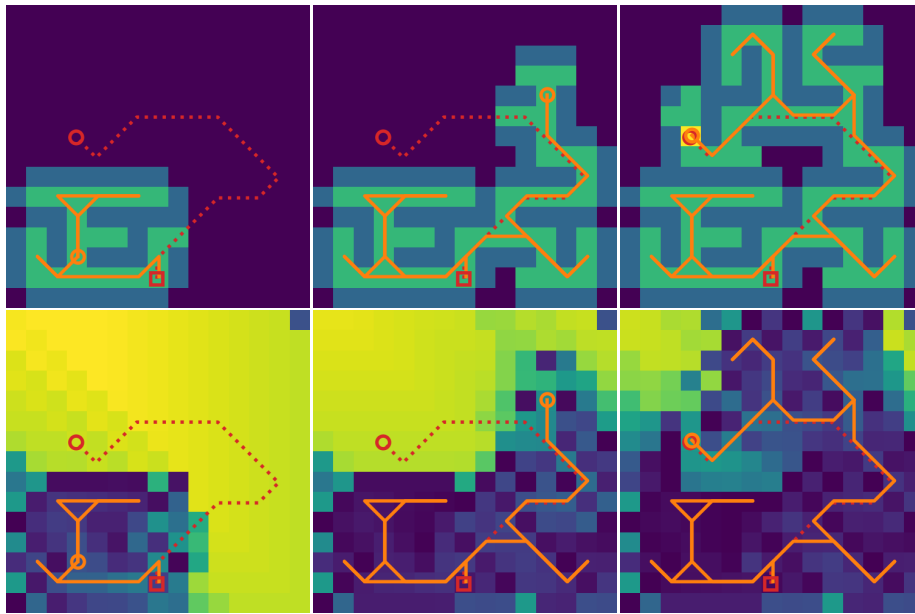


Figure 6: Example rollout of CALVIN after 21 steps (left column), 43 steps (middle column) and 65 steps (right column). CALVIN successfully terminated at 65 steps. **(top row)** Input visualisation: unexplored cells are dark, the discovered target is yellow. The correct trajectory is dashed, the current one is solid. The orange circle shows the position of the agent. **(bottom row)** Predicted values (higher values are brighter). Explored cells have low values, while unexplored cells and the discovered target are assigned high values.

A.7.1 Rollout of CALVIN

Figure 7 shows an example of a trajectory taken by CALVIN at runtime, with corresponding observation maps, predicted values and predicted rewards for taking the “done” action. Similarly to appendix A.6, the agent manages to explore unvisited cells and backtrack upon a dead end until the target is discovered. One key difference is that now the agent learns to predict rewards and values for every discretised orientation as well as the discretised location. Upon closer inspection, we observe that the predicted values are higher facing the direction of unexplored cells and towards the discovered target. Since rotation is a relatively low cost operation, in this training example, the network seems to have learnt to assign high rewards to a particular orientation at unexplored cells, from which high values propagate. Rewards and values averaged over orientations yield a more intuitive visualisation.

A.7.2 Rollout of VIN

A corresponding visualisation for VIN is shown in fig. 8. Unlike CALVIN’s implementation of rewards (eq. 5 in sec. 4.1) as a function of discretised states and actions, the “reward map” produced by the VIN does not offer a direct interpretation, as it is shared across all actions as implemented by Tamar et al.[5], and is also shared across all orientations in the case of embodied navigation. The values are also not well learnt, with some of the higher values appearing in obstacle cells. The unexplored cells are not assigned sufficiently high values to incentivise exploration by the agent. In this example, the agent gets stuck and starts oscillating between two orientations after 57 steps.

A.7.3 Rollout of GPPN

Finally, a visualisation for GPPN is shown in fig. 9. Unlike VIN and CALVIN, GPPN does not have an explicit reward map predictor, but performs value propagation using an LSTM before outputting a final Q-value prediction. Similarly to appendix A.7.2, the values predicted is not very interpretable, and does not incentivise exploration or avoidance of dead ends. In this example, the agent keeps revisiting a dead end that has already been explored in the first 20 steps.

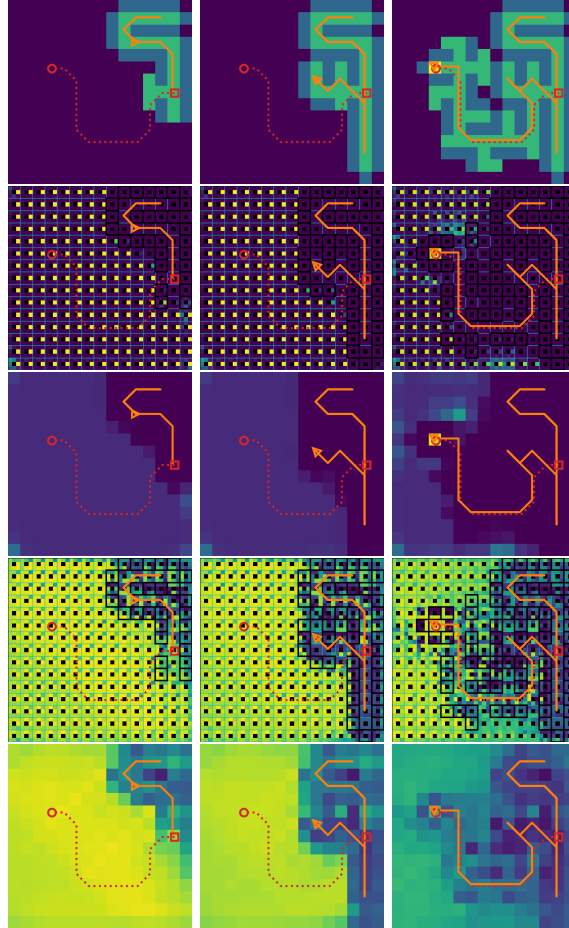


Figure 7: Example rollout of embodied CALVIN after 30 steps (left column), 60 steps (middle column) and 90 steps (right column). CALVIN successfully terminated at 91 steps. **(first row)** Input visualisation: unexplored cells are dark, the discovered target is yellow. The correct trajectory is dashed, the current one is solid. The orange triangle shows the position and the orientation of the agent. **(second row)** Predicted rewards (higher values are brighter). The 3D state-space (position/orientation) is shown, with rewards for the 8 orientations in a radial pattern within each cell (position). Explored cells have low rewards, while unexplored cells and the discovered target are assigned high rewards. **(third row)** Predicted rewards averaged over the 8 orientations. **(fourth row)** Predicted values following the same convention. Values are higher facing the direction of unexplored cells and the target (if discovered). **(fifth row)** Predicted values averaged over the 8 orientations.

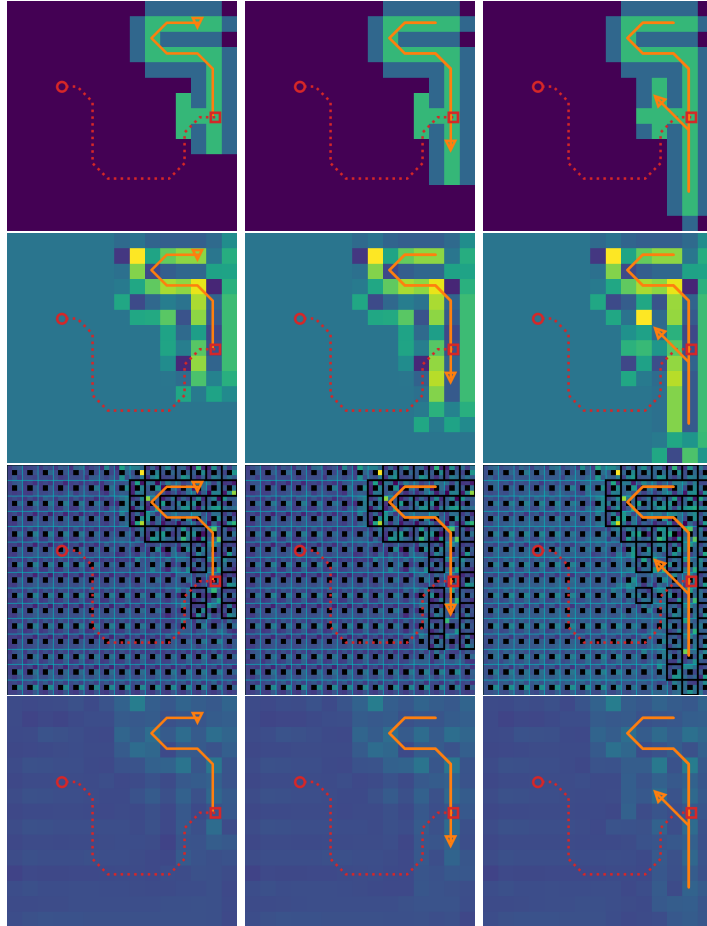


Figure 8: Example rollout of embodied VIN after 20 steps (left column), 40 steps (middle column) and 60 steps (right column). VIN kept oscillating between the same two states after 57 steps. The convention is the same as for fig. 6, except that a single reward map is shared across all orientations. **(first row)** Input visualisation. **(second row)** Predicted rewards. **(third row)** Predicted rewards averaged over the 8 orientations. **(fourth row)** Predicted values. **(fifth row)** Predicted values averaged over the 8 orientations.

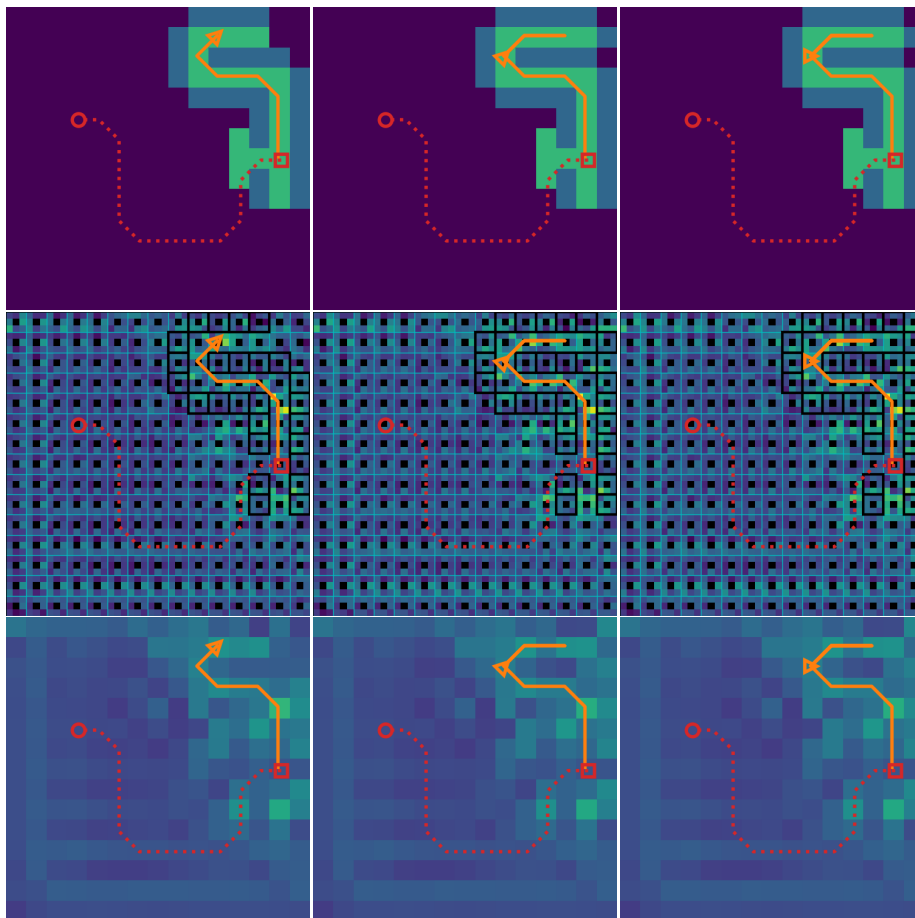


Figure 9: Example rollout of embodied GPPN after 15 steps (left column), 30 steps (middle column) and 45 steps (right column). GPPN revisits the same sequences of states leading to a dead end after 45 steps. The convention is the same as for fig. 6. **(first row)** Input visualisation. **(second row)** Predicted rewards. **(third row)** Predicted rewards averaged over the 8 orientations. **(fourth row)** Predicted values. **(fifth row)** Predicted values averaged over the 8 orientations.